RSC Advances

PAPER

View Article Online
View Journal | View Issue

Cite this: *RSC Adv.*, 2019, **9**, 31177

Synthesis of 3D flower-like structured Gd/TiO$_2$@rGO nanocomposites *via* a hydrothermal method with enhanced visible-light photocatalytic activity

Shuaiqiang Jia,[a] Jinlong Li,*[ab] Guozhe Sui,*[ab] Lijuan Du,[a] Yulin Zhang,[a]
Yan Zhuang[a] and Boxin Li[a]

Received 4th August 2019
Accepted 23rd September 2019

DOI: 10.1039/c9ra06045f

rsc.li/rsc-advances

In this study, novel Gd/TiO$_2$@rGO (GTR) nanocomposites with high photocatalytic performance were fabricated *via* a one-pot solvothermal approach. During the preparation step, graphene oxide (GO) was reduced to reduced graphene oxide (rGO), and subsequently, on the surfaces of which anatase TiO$_2$ doped with Gd metal was grown *in situ* with a 3D petal-like structure. Gd doping into the classical TiO$_2$@rGO system efficiently expands the absorption range of light, improves the separation of photogenerated electrons, and increases the photocatalytic reaction sites. The specific surface areas, morphological structures, and valence and conduction bands of the obtained GTR nanocomposites were analyzed and correlated with their enhanced photocatalytic performances for the degradation of an aqueous RhB solution. The experimental results indicated that the best performance was achieved with the 3% GTR composite, which exhibited the highest photoelectrocatalytic activity because of two aspects: the rapid separation of electrons and holes, and improvement in adsorption capacity. As compared with pure TiO$_2$, the GTR composites demonstrated enhanced photoactivity due to synergetic effects between the effective photo-induced electron transfer from TiO$_2$ to the surface of the rGO acceptor through interfacial interactions and the variation of structure and electrons under the adoption of Gd.

1. Introduction

In recent years, photocatalysis technology using semiconductors has drawn significant attention from researchers because it is one of the most effective ones for the decomposition of pollutants present in aqueous media.[1,2] Among various semiconductors, TiO$_2$ has been considered one of the most representative photocatalysts owing to its strong oxidizing power,[3] photostability,[4] and relative non-toxicity.[5] Nevertheless, anatase TiO$_2$ possesses a wide band gap energy (~3.2 eV) that limits its utilization of natural sunlight and photoactivity under UV light (<387 nm) due to fast electron–hole recombination. UV radiation comprises around 3 to 5% of the sunlight at Earth's surface.[6,7] Thus, researchers are focusing on extending the absorption spectrum of TiO$_2$ from UV to the visible-light region to exploit the visible light occupying 42–43% of sunlight.[8,9] Recently, researchers have modified TiO$_2$ with carbon-containing materials such as carbon nanotubes,[10–13] graphitic carbon nitride (g-C$_3$N$_4$),[14–17] and graphene,[18–21] which have high carrier mobilities and large specific surface areas; this strategy is considered as an effective way to further strengthen the photocatalytic activities of TiO$_2$ catalysts.

Compared with other carbon materials, graphene is a crystalline allotrope of carbon with a two-dimensional structure,[22,23] and is both the thinnest and the strongest material measured so far in the world.[24,25] Graphene can be used in many applications such as new energy materials, energy conversion, and tissue engineering. Owing to its high electron mobility,[26] lower resistivity,[27] extended π–π conjugation structure,[28] and faster electron transfer ratio,[29,30] graphene has attracted increasing attention recently. Because of this, graphene can be easily combined with nanostructured materials to form some semiconductor-supported compounds.[31] Therefore, several methods have been used to combine TiO$_2$ and graphene to improve the photodegradation efficiency of TiO$_2$, including hydrothermal, physical mixing, sol–gel, and electrochemical deposition.[32] A large number of TiO$_2$/graphene composites with different structure have been designed and prepared to improve the photocatalytic activity of TiO$_2$; the combination of graphene with TiO$_2$ not only reduces the electron–hole recombination by transferring the photoexcited electron to the graphene surface,

---

[a] *College of Chemistry and Chemical Engineering, Qiqihar University, Qiqihar 161006, China. E-mail: jinlong141@163.com; suiguozhe@163.com; Fax: +86-452-2738205; Tel: +86-452-2738205*

[b] *Heilongjiang Provincial Key Laboratory of Catalytic Synthesis for Fine Chemicals, Qiqihar 161006, China*

but also enlarges the absorption band of pure TiO_2 to the visible region and enhances the surface area of TiO_2.[33–35]

Additionally, to enhance the photocatalytic activity of TiO_2, many researchers have focused on metal-loaded TiO_2 materials to expand to visible-light-response region *via* the induction of impurity levels. Liu *et al.*[36] synthesized a small particle size of Ga–TiO_2 composite powders with high specific surface area by a mild hydrothermal method; the synthesized photocatalyst exhibits better photocatalytic activity than that of commercial P25 TiO_2 or undoped TiO_2. Chen *et al.*[37] investigated the higher photoactivity of a TiO_2/diatomite with co-doped Ce/N granule than that of a single N-doped granule through the sol–gel way by evaluating the degradation efficiency of oxytetracycline under visible-light illumination. Muhammad *et al.*[38] prepared Gd/SnO_2–TiO_2 nanoparticles by using ultrasonic and hydrothermal methods, and investigated the effect of Gd concentration on band gap, which revealed a red shift from 5.3 to 2.0 eV for Gd/SnO_2–TiO_2. All these methods provide notable improvements in the photocatalytic property of TiO_2. However, there is no report on the investigation of Gd-loaded TiO_2 on rGO (Gd/TiO_2@rGO; GTR) photocatalysts.

In this work, we selected graphene as the support material to enhance the synergistic effect between TiO_2 and Gd, and synthesized GTR photocatalysts *via* a convenient and fast one-pot method for synthesizing photocatalytic materials. Graphene was used not only to improve the adsorbability of organic contaminants, but also to induce a positive relationship between Gd and Ti species. In order to investigate the photocatalytic activities of the as-synthesized GTR composites, the photodegradation of Rhodamine B (RhB) was performed in aqueous solution. And the reusability of GTR composites was also examined in this work.

2. Experimental

2.1 Reagents

Graphite powder (purity > 99.9%), sulfuric acid (H_2SO_4, 98.0 wt%), potassium permanganate ($KMnO_4$), hydrogen peroxide (H_2O_2, 30.0 wt%), sodium nitrate ($NaNO_3$), hydrochloric acid (HCl, 36.5 wt%), hydrofluoric acid (HF, 40 wt%), and absolute ethanol (CH_3CH_2OH) were analytical-grade reagents. Tetrabutyl titanate (TBT, $C_{16}H_{36}O_4Ti$, 98.0%) was used as a titanium precursor to synthesize the TiO_2 nanocrystals. Rhodamine B (RhB, $C_{28}H_{31}N_2O_3Cl$) was selected to evaluate the photocatalytic degradation efficiency of dyestuff. All the above chemicals were obtained from Tianjin Kemiou Chemical Reagent Co. (Tianjin, China). Gadolinium(III) nitrate hexahydrate ($GdN_3O_9 \cdot 6H_2O$, 99.0%) was purchased form Aladdin Chemistry Co. Ltd. The used deionized (DI) water in all experiments was generated from a UPE-60 water purification system (Beijing Sanda Technology Co., Ltd). All reagents were used without further purification.

2.2 Synthesis of GO

GO was prepared through the modified Hummers' method. In a typical synthesis, 2 g of graphite powder and 1.0 g of $NaNO_3$ were poured into a round-bottom flask and 46 mL of concentrated H_2SO_4 was slowly added to it. The mixture was kept stirring for 1 h with magnetic stirrers. Subsequently, 6.0 g $KMnO_4$ was slowly added to the mixture and stirred for 2 h for uniform stir. During the above synthetic processing, an ice bath apparatus was used to prevent temperature from exceeding 10 °C. Thereafter, the reaction temperature was adjusted to 35 °C and continuously stirred for another 0.5 h. Then, 160 mL of distilled water was carefully added and the resulting mixture was stirred at 98 °C for 0.5 h. During the reaction, the color of the mixture changed from snuff color to bright yellow. Afterward, 30 mL H_2O_2 was slowly fed into the mixture with stirring for 0.5 h, during which plenty of bubbles evolved. The resulting bright yellow mixture was centrifuged, and the precipitate was washed with a 5% HCl aqueous solution until no metal ions remained and then washed thoroughly with deionized water to neutral pH. The obtained GO mud was dried in a vacuum oven at 60 °C.

2.3 Synthesis of Gd/TiO_2@rGO

GTR was synthesized through an efficient one-step solvothermal route. A solution of GO nanosheets was obtained after that 0.1 g of GO was dissolved in 30 mL of isopropyl alcohol by sonication for 30 min. Then, the mixture added by 1 mL of TBT was sonicated for another 30 min to form a homogeneous solution. Next, 0.5 mL of HF (40 wt%) was dropped into the solution under continuous stirring. Meanwhile, 1.8 mL of a $Gd(NO_3)_3$ aqueous solution (0.5 mol L^{-1}) was dispersed into the above solution and magnetically stirred for 20 min to ensure uniform distribution. Finally, the mixed solution was put into a Teflon-lined stainless steel autoclave and then treated at 180 °C for 10 h. At the end of this process, the obtained product from the autoclave was washed with deionized water and absolute ethanol several times, and dried in a vacuum oven at 60 °C for 24 h. A series of GTR composites was synthesized by varying the volumes of $Gd(NO_3)_3$ and TiO_2. For comparison, TiO_2@rGO nanosheets were prepared without Gd by the above mentioned solvothermal method.

2.4 Characterization

Scanning electron microscopy (SEM) images were taken with a Hitachi S-3400 system (Tokyo, Japan) operated at 100 kV, and transmission electron microscopy (TEM) images were taken with a Hitachi system (Tokyo, Japan) operated at 200 kV. X-ray diffraction (XRD) analysis was performed on a Bruker D8 system (Germany) to determine the crystal structure and the phase compositions of the samples equipped with Cu K_α radiation under 40 kV and 30 mA. And the patterns were recorded in the range of $2\theta = 10–80°$ with a speed of 4.00° min^{-1}. UV-visible diffused reflectance spectra were obtained for the dry-pressed disk samples using a UV-visible spectrophotometer (Du800, Beckman Co.) with $BaSO_4$ as a reflectance standard. The Brunauer–Emmett–Teller (BET) analysis were carried out to determine the specific surface areas of the samples using a N_2 adsorption–desorption apparatus (Nova 2000e, Quantachrome Co.) with the relative pressure ranging from 0.05–0.35, and the samples were previously degassed at 300 °C for 3 h under vacuum. The Barrett–Joyner–Halenda (BJH) approach was used to determine the pore size distribution of the photocatalysts. Fourier transform infrared (FT-IR) spectra were measured to determine the functional groups with a Nexus 670 (Nicolet Co.) FT-IR spectrophotometer using the KBr pellet technique. X-ray photoelectron spectroscopy (XPS) was performed on an Axis Ultra DLD (Krotos Co., UK). The photoelectron take-off angle was kept at 45°, and the binding energy was carefully referring to the C 1s peak by setting at 285.0 eV.

2.5 Evaluation of photocatalytic activity

RhB as one of the most important representative organic dyestuff has been well applied in industrial production, which seriourslycontaminates the surrounding environment. Hence, we chose it as a representative pollutant to evaluate the photocatalytic activities of the GTR composites by photo-degradation of an aqueous solution of RhB dye under visible-light illumination. A 500 W Xe lamp was employed as the light source, and the visible wavelength was adjusted using a UV-cut filter (420 nm). The experiments were performed with 50 mg of the porous TiO_2 photocatalyst and a solution of RhB (50 mL; 10 mg L^{-1}) in a tube reactor. The suspension of the RhB solution and photocatalyst was magnetically stirred in the dark for 60 min to ensure establish an adsorption/desorption equilibrium before irradiation. Then, visible light was directed towards the suspension. Aliquots of samples were withdrawn from the suspension at regular time intervals (30 min) and centrifuged to separate the catalyst powder using a high-speed rotation of centrifuge rotor (RG-TGL-16C, Ruijiang Co.). The absorbance of collected filtrate was measured to calculate the RhB degradation efficiency by UV-vis spectrophotometry (SP 1900, Shanghai Spectrum Instruments Co.) using the representative peak of RhB at 552.0 nm.

2.6 Recycling test

After each photocatalytic experiment, the synthesized GTR composites were recycled by repeated centrifuging and washing with ethanol. The recycled GTR composites were used as photocatalysts to degrade RhB (10 mg L^{-1}) solution under visible-light illumination, respectively. In this recycling test, the reusability of 3% GTR composite was investigated by repeating the experiment five times.

3. Results and discussion

3.1 Characterization

The TEM and SEM images clearly show the morphology, structure and size of the as-synthesized composites (Fig. 1). The TEM image of GO shown in Fig. 1(a) clearly illustrates the typical flake-like shapes of GO with wrinkles, which is attributed to the thin and large sheets of GO. Here, the 3% GTR sample was chosen as a representative composite as it demonstrated the best photocatalytic performance toward RhB photodegradation. As seen from the TEM image in Fig. 1(b), well-dispersed Gd/TiO_2 nanoparticles are wrapped tightly onto the surface of rGO sheets. This implies that TiO_2 nanoparticles were successfully deposited onto the GO surface by the hydrothermal method, resulting in the formation of large GTR composites. The diameters of the TiO_2 nanoparticles deposited onto the GO surface ranged from 150 to 250 nm. All the precursors exhibited very similar and uniform spherical morphologies. Fig. 1(d) shows that the morphology of TiO_2 nanoparticles is petaloid ambulacra, and many TiO_2 nanosheets assemble into a 3D petalage-like structure.

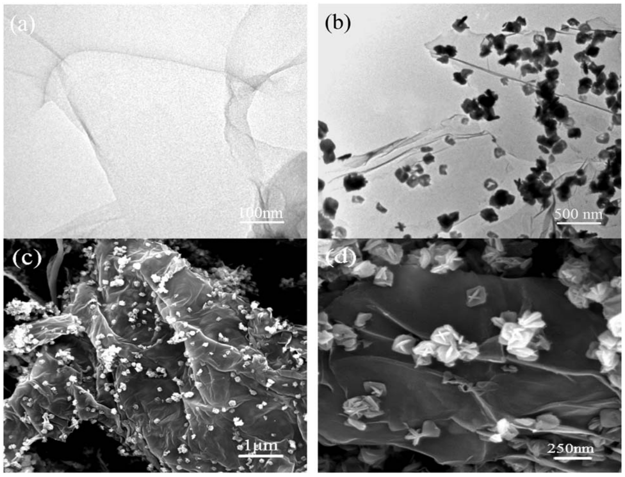

Fig. 1 TEM images of (a) GO nanosheets and (b) 3% GTR sample. (c) and (d) SEM images of 3% GTR composite.

The elemental maps of C, Ti, and Gd in the 3% GTR sample are shown in Fig. 2(b–d), respectively. It is observed that massive C and Ti nanoparticles are dispersed uniformly among the rGO sheets in the composite. Besides, a small amount of Gd nanoparticles can be observed in Fig. 2(d). The small amount of

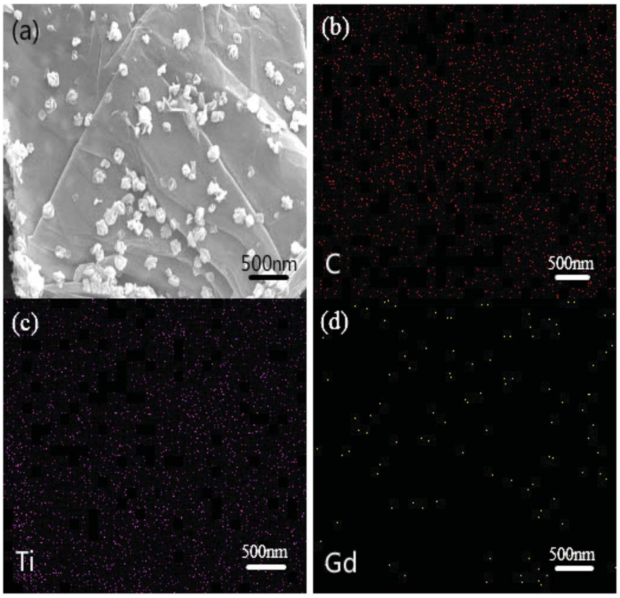

Fig. 2 Elemental maps of (b) C atoms, (c) Ti atoms, and (d) Gd atoms in the same area of 3% GTR composite shown in (a).

Gd nanoparticles plays an important role in the photocatalytic performance of the GTR, which will be discussed in a later section.

The XRD profiles of GO, pure TiO_2, and GTR composites containing different amounts of Gd are shown in Fig. 3. The peak at 12.6° in the profile of the GO sample corresponds to the (002) crystal plane, indicating that graphite has considerably oxidized into GO. After the solvothermal treatment, this strong characteristic diffraction peak of GO almost disappeared but only a weak diffraction peak appeared at 24.0°, suggesting that most of GO was reduced, which is a clear indication of the conversion of GO to rGO. In the hydrothermal experimental conditions, the synthesized anatase TiO_2 has a perfect crystal structure, as observed from the XRD results. The GTR composites show peaks at $2\theta = 25.1°$, 38.2°, 48.0°, 53.9°, 54.9°, 62.8°, 68.9°, 70.1°, and 75.0°, corresponding to the (101), (004), (200), (105), (211), (204), (116), (220), and (215) crystal planes, which can be well indexed to anatase TiO_2 (JCPDS card no. 21-1272), as shown in Fig. 3. The result demonstrates that the obtained nanocomposites exhibit similar XRD profiles as that of the pure TiO_2. The average nanocrystal sizes (D in nm) of the GTR samples were evaluated by the Scherrer formula based on the (101) XRD peak broadening, $D = k\lambda/\beta\cos\theta$, where k is the Scherrer constant that depends on the particle shape ($k = 0.89$), λ is the X-ray radiation wavelength (0.154056 nm), β is the full width half-maximum (FWHM) of the most intense peak, and θ is the Bragg diffraction angle. The average particle diameter of the TiO_2 nanostructures is given in Table 1. We can clearly see in the XRD profiles that amorphous TiO_2 transforms into the crystalline anatase phase during the hydrothermal process of combining with GO, resulting in intense and clearly visible peaks belonging to anatase TiO_2. Thus, for these composites, the temperature of 180 °C, which was used for the hydrothermal reduction of GO, was found to be sufficient to transform amorphous TiO_2 into the anatase crystalline form.

Fig. 4 illustrates the N_2 adsorption–desorption isotherms and the corresponding pore size distribution curves of pure TiO_2 and the GTR composites containing different amounts of Gd. Following the IUPAC classification, all the adsorption–desorption isotherms of the samples were considered to be type IV curves with a clear H1 hysteresis loop, which reflect the mesoporous structures existing in the synthesized GTR materials as well as facile connectivity between the pores. The high adsorption amount in the initial step of the hysteresis loop corresponding to the capillary condensation of Gd inside the mesopores reveals a narrow pore-size distribution of the GTR materials.[39] The specific surface area, pore volume, and pore size of different samples were calculated, and the data are summarized in Table 1. For pure TiO_2, GO@TiO_2, 2% GTR, 3% GTR, and 4% GTR, the specific surface areas are determined as 49.0, 119.6, 122.7, 125.6, and 112.7 $m^2\ g^{-1}$, the total pore volumes are 0.25, 0.31, 0.34, 0.35, and 0.37 $cm^3\ g^{-1}$, and the pore sizes are 7.22, 4.61, 3.82, 3.84, and 4.32 nm, respectively. It is interesting to observe that when GO was combined, the specific surface area and pore volume increased as compared with those of pure TiO_2, respectively. Furthermore, the BET characteristic results suggested that the increased Gd content results in a slight improved surface area of the GTR composite, which can facilitate photocatalysis owing to the improved adsorbability. With the content of metal Gd increasing, it may affect the folding degree of carrier material after hydrothermal reaction. This result can be ascribed to the Gd formation on the carbon (GO) edge, which leads to the volumetric expansion of pore.[40] Therefore, it should be mentioned that the surface area, pore volume, and pore size have a definite effect on the photocatalytic activity.

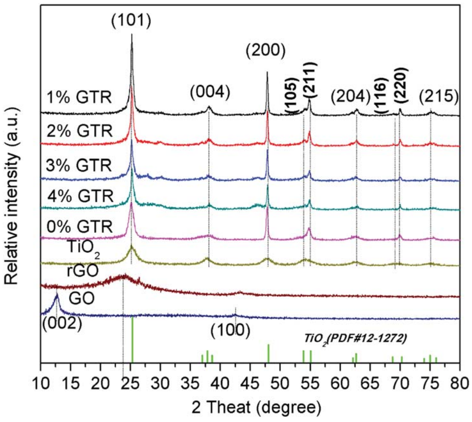

Fig. 3 XRD profiles of GO, pure TiO_2 and GTR composites with different.

To confirm the presence of Ti^{3+} defects and further prove the successful doping of Gd ion, XPS spectra were measured to determine the chemical states of the 3% GTR sample. Fig. 5(a) shows the full-scale XPS profile of the 3% GTR sample, which indicates the chemical binding energies of approximately 459.6 eV, 530.3 eV, 284.8 eV, and 144.2 eV correspond to Ti 2p 3/2, O 1s, C 1s, and Gd 4d, respectively. As shown in Fig. 5(b), the C 1s core-level spectrum of the 3% GTR composite can be devolved into four peaks at 284.7, 285.4, 286.3, and 289.0 eV, which are closely assigned to C=C, C–C, C–O (hydroxyl or epoxy), and C–O–Ti, respectively. The presence of Ti–O–C structure disclosed that some of the Ti atoms were substituted with the C atoms in the TiO_2 lattice during the preparation process. The O 1s spectra are displayed in Fig. 5(c), which show three peaks corresponding to the Ti–O–Ti bond (530.6 eV), Ti–O–H bond (531.3 eV), and C–OH species (532.7 eV), respectively. Fig. 5(d) shows the spectra of Ti 2p, wherein two main peaks are observed at 459.6 eV (Ti 2p 3/2) and 465.3 eV (Ti 2p 1/2). These binding energy values are in agreement with those of TiO_2. Moreover, the difference between these two binding energies represents the standard binding energy of Ti element. The Ti 2p 3/2 peak shifted slightly toward higher zone of binding energy; this shift may be explained by a variation in the chemical state and coordination structure of Ti 2p 3/2 owing to the interactions between rGO and TiO_2. In Fig. 5(e), the peak centered at 144.2 eV could be owing to the presence of Gd 4d 5/2. It was reported that the binding energy of Gd 4d 5/2 in Gd_2O_3 is 142.1 eV.[41,42] Therefore, our experimental data shows a higher binding energy than that of Gd_2O_3, which indicates that Gd exists in the form of Gd^{3+}, and the chemical environment of

Table 1 Parameters obtained from nitrogen desorption isotherm experiments by BET and BJH methods and average anatase crystallite size of the composites

Sample	Pore diameter, D_{BJH} (nm)	Pore volume, V_{TOTAL} (cm^3 g^{-1})	Surface area, S_{BET} (m^2 g^{-1})	Anatase crystallite size, D (nm)
Pure TiO_2	7.22	0.25	49.0	11.3
GO@TiO_2	4.61	0.31	119.6	8.6
2% GTR	3.82	0.34	122.7	8.9
3% GTR	3.84	0.35	125.6	8.1
4% GTR	4.32	0.37	112.7	7.2

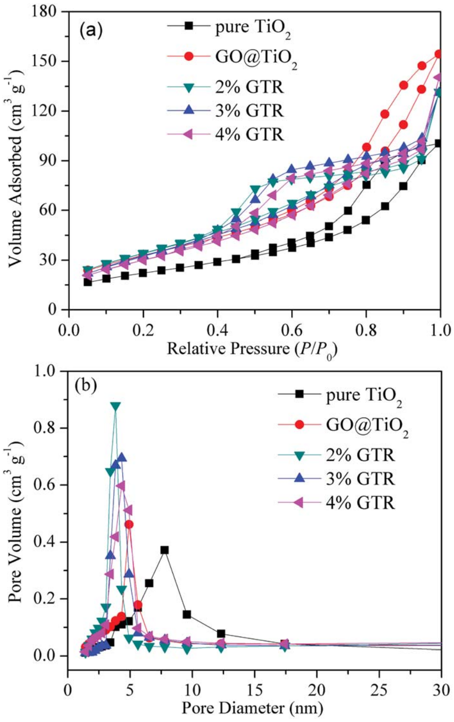

Fig. 4 (a) N_2 adsorption–desorption isotherms and (b) pore size distribution curves of pure TiO_2 and GTR composites with different amounts of Gd.

Gd^{3+} in the 3% GTR sample changed, possibly because of the formation of Gd–O–Ti linkages.[43]

The FTIR spectra of GO, TiO_2@rGO, 3% GTR composite, and TiO_2 samples are presented in Fig. 6. The bands in the spectra of GO, TiO_2@rGO, and 3% GTR composites appearing at 1120, 1570, and 1610 cm^{-1} arose from the stretching vibrations of oxygen-containing functional groups, such as C–O–H/C–O–C, C=C, and carbonyl C=O. The broad band located at around 3420 cm^{-1} originates from the OH stretching vibrations. It can be seen that the spectrum of GO exhibits many strong absorption peaks corresponding to various oxygen-containing functional groups. The spectra of TiO_2@rGO, 3% GTR composite, and TiO_2 samples show strong and wide peaks in the range of 450 to 1000 cm^{-1}, which correspond to the bending vibrations of Ti–O–Ti bonds. The bands of oxygen-containing groups clearly observed in the GO spectrum changed in the spectra of 3% GTR composites, which indicates that GO was successfully reduced during the hydrothermal preparation.[44,45] The above results indicate that the reduction of GO takes place in the TiO_2 and rGO phases *via* bridging oxygen in both TiO_2@rGO and the 3% GTR composite.

Fig. 7 displays the diffuse reflectance absorption spectra of pure TiO_2 and the as-prepared GTR samples. It is seen that the GTR samples exhibit a red shift in the photoabsorption edge with increasing content of Gd along with a strong optical absorption in the visible-light region range.[46] The curves in Fig. 7(a) displays the DRS spectra of TiO_2, GO@TiO_2, 1% GTR, 2% GTR, 3% GTR, and 4% GTR powders from bottom to top, respectively. It can be observed that the introduction of rGO and Gd ions in the GTR with gray color extends its absorption to the visible-light region and enhances visible-light absorption ability. A plot of the transformed Kubelka–Munk function as a function of energy of light is shown in Fig. 7(b), from which the band gaps of GO@TiO_2, 1% GTR, 2% GTR, 3% GTR, and 4% GTR are roughly estimated as 2.82, 2.51, 2.41, 2.38, and 2.24 eV, respectively. This reveals that a qualitative observation of a red shift of the photoabsorption edge of the GTR composites as compared to pure TiO_2.

3.2 Photocatalytic activity and reusability

The photocatalytic activities of the as-synthesized composites were evaluated by the degradation of RhB under visible-light illumination. The visible light was turned on to initiate the photocatalytic reaction for 180 min after the adsorption–desorption equilibrium was reached within 60 min of stirring in a dark environment. The photocatalytic activities of different samples were determined and the experimental results are shown in Fig. 8.

The as-synthesized GTR composites are well dispersed in an aqueous continuous phase for the removal of the RhB dye during the pre-adsorption process because of the hydrophilic property of rGO. After stirring for 60 min, the adsorption equilibrium had been almost reached. The adsorption percentages of RhB for the synthesized GTR photcatalysts and pure TiO_2 were around 61% and 6%, respectively. As shown in Fig. 8, the photoactivity of the GTR composite was higher than that of pure TiO_2. The removal efficiencies of the GTR samples with Gd doping ratios of 1, 2, 3, and 4% were determined as 88.3, 86.9, 91.5, and 85.9%, respectively, after visible-light irradiation for 180 min. After photodegradation process, the blank experiment result showed that the dye on its own for the full duration of the experiment were stability.

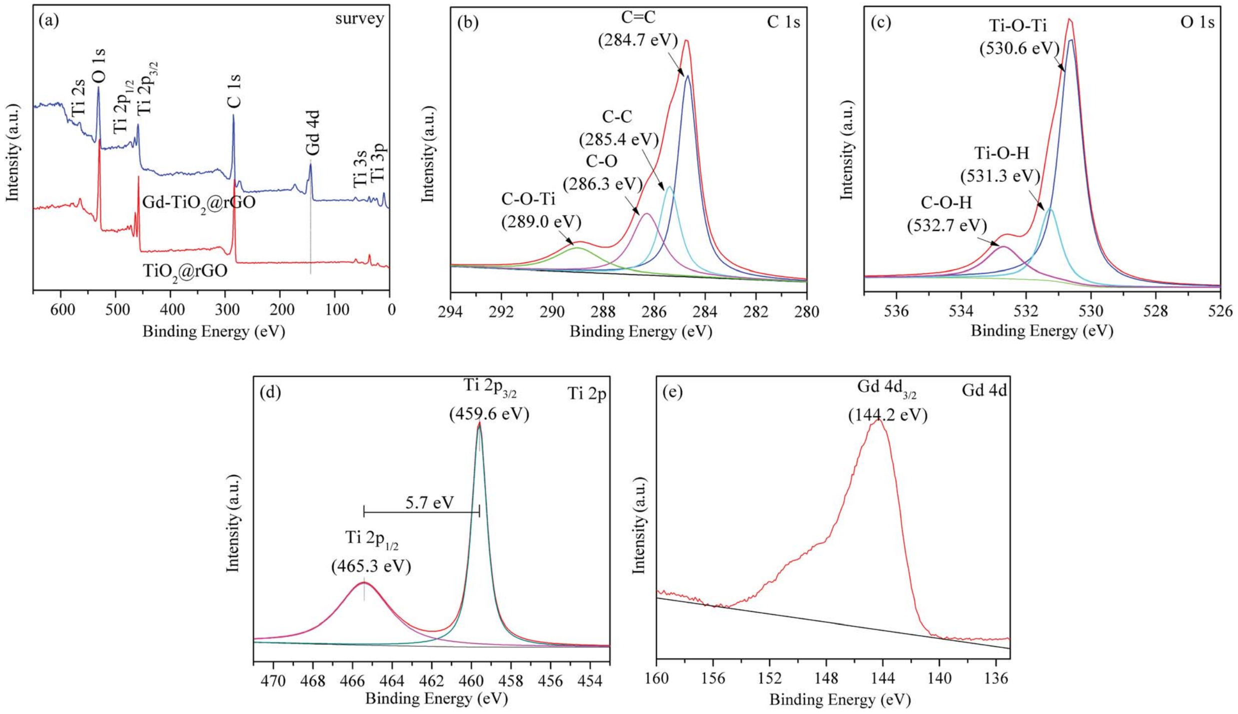

Fig. 5 XPS survey spectra (a); C 1s (b), O 1s (c), Ti 2p (d), and Gd 4d (e) XPS spectra of 3% GTR composite.

We adjusted the Gd content in the GTR composite to determine the influence of Gd on the photodegradation performance. The 3% GTR composite afforded a 3.5 times higher apparent rate constant for the photodegradation of RhB than that of pure TiO_2. It is well known that GO has been studied to be a competitive acceptor material owing to its two-dimensional π-conjugated structure.[47] Such structures can improve the conductivity and transport of charge carriers of the GTR composite.[48] For this reason, photo-induced electrons could rapidly transfer from the conduction band of TiO_2 to rGO through interfacial interactions. It can suppress the recombination rate of electron–hole (e^-–h^+) pairs in the composite system, generating more charge carriers to react with the RhB

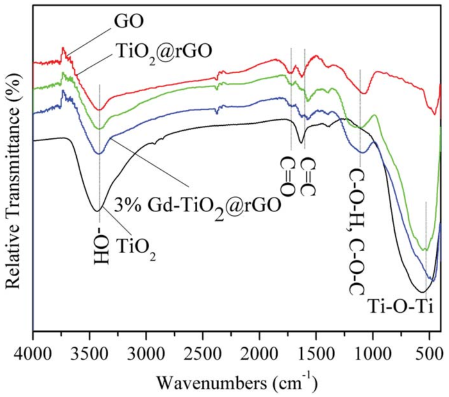

Fig. 6 FTIR spectra of some samples.

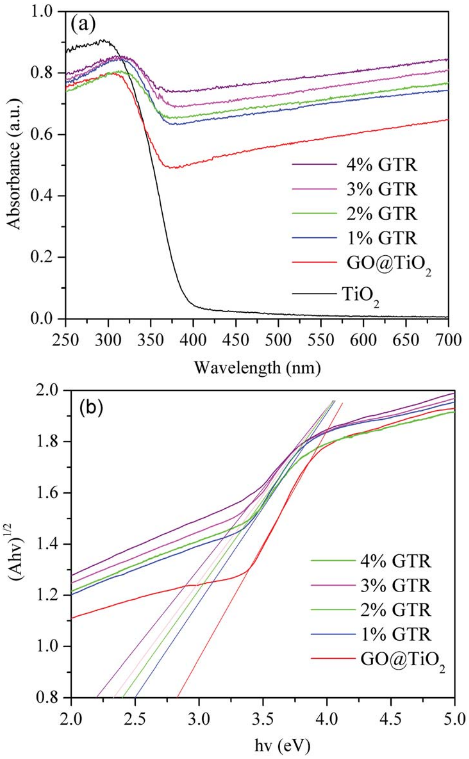

Fig. 7 (a) UV-vis diffuse reflectance spectra of the synthesized photocatalysts in different doping ratios. (b) Plot of transformed Kubelka–Munk function *versus* the energy of light for GTR composites with different Gd contents.

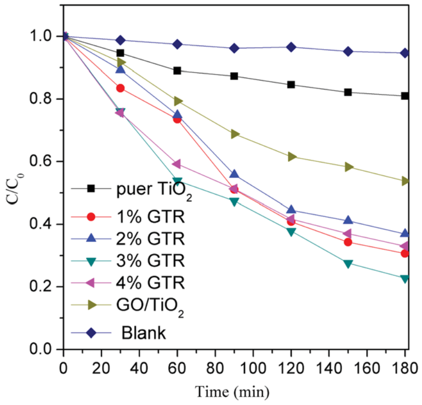

Fig. 8 Photocatalytic activities of pure TiO_2 and GTR photocatalysts with different doping ratios.

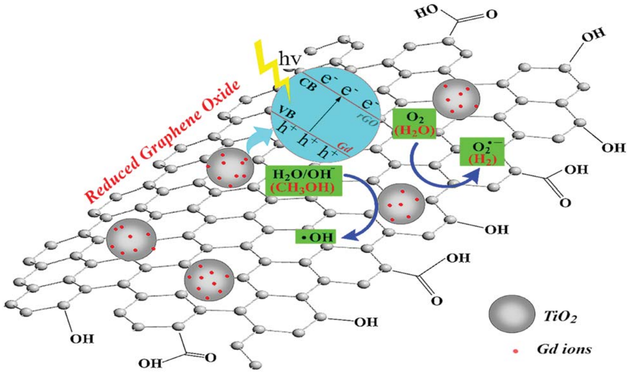

Fig. 10 Schematic illustration of photodegradation of RhB by GTR composites under irradiation by visible light region of the simulated sunlight.

dye molecules.[49,50] The superior performance of GTR, therefore, can be largely assigned to the effective charge transport of the photogenerated electrons in RhB and TiO_2 to graphene and Gd nanoparticles.

Fig. 9 shows the adsorption and photocatalytic performance of the 3% GTR composite for a RhB (10 mg L^{-1}) solution after eight repeated experiments, in which the composites were reused after washing with ethanol at least eight times in each cycle until the degradation reaches stable. The results show that after eight cycles, the removal efficiency of RhB by GTR decreases to 76.65%, suggesting that the obtained GTR composite has good stability. This indicated that the GTR composites could be applied as a suitable candidate for treating with sewage water in environmental.

3.3 Mechanism of degradation

Fig. 10 presents a schematic diagram of the photocatalytic degradation of RhB by the GTR photocatalyst. Based on the characterization and photodegradation results, we can assume that both electrons (e^-) and holes (h^+) can interact with O_2 and H_2O to form superoxide ($O_2^{\bullet-}$) and hydroxyl radicals (·OH).[51] The Gd/TiO_2 petaloid ambulacra attached to the graphene sheets transmit their activated electrons to the rGO due to band arrangement, which prevent the recombination of electron–hole. The generated large electric field promotes the light-induced electron orientation of rGO to the interface between Ga and TiO_2, and the electron–hole recombination is effectively prevented in this process. Thus, during the photocatalytic reaction, holes and superoxide are the most important active species, which is consistent with the results of the active component trapping experiment.

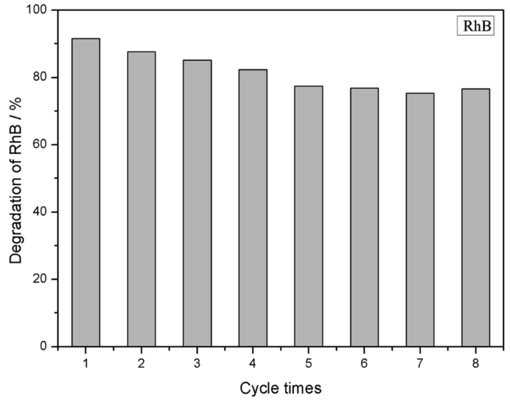

Fig. 9 Recycling of 3% GTR photocatalyst for RhB dye removal.

Herein, both Gd nanoparticles and graphene are excellent co-catalysts, and we propose that their presence increases the total reaction sites of the system and synergistically contributes to TiO_2, thus significantly improving the photodegradation of RhB and hydrogen generation. The mechanism can be described as eqn (1)–(7).

$$\text{GTR} + \text{RhB} \rightarrow \text{GTR–RhB} \tag{1}$$

$$\text{rGO/TiO}_2 + h\nu \rightarrow \text{rGO/TiO}_2\ (\text{h}^+ + \text{e}^-) \tag{2}$$

$$\text{Gd} + h\nu \rightarrow \text{Gd}\ (\text{h}^+ + \text{e}^-) \tag{3}$$

$$\text{e}^- + \text{O}_2 \rightarrow \text{O}_2^{\bullet-} \tag{4}$$

$$\text{h}^+ + \text{OH}^- \rightarrow \cdot\text{OH} \tag{5}$$

$$\text{O}_2^{\bullet-} + \text{H}_2\text{O} \rightarrow \cdot\text{OH} \tag{6}$$

$$\cdot\text{OH} + \text{RhB} \rightarrow \text{CO}_2 + \text{H}_2\text{O} \tag{7}$$

4. Conclusion

In conclusion, we prepared GTR composites *via* a simple and efficient one-pot solvothermal method. The characterization results (FTIR and XPS) showed that GO was successfully reduced to rGO during the hydrothermal process and perfect Ti–O–C bonds existed between TiO_2 and rGO. The results showed that all the as-prepared GTR composites performed better in the photodegradation of RhB in simulated wastewater than the pure TiO_2 nanoparticles, which revealed that the obtained rGO could be used as an effective co-catalyst to improve the photocatalytic performance of TiO_2. We also proposed that the Gd nanoparticles played an important role in enhancing the photocatalytic ability of the GTR composite by expanding the absorption to the visible region, which may increase the amount of reaction site and facilitate charge separation and transfer under UV-vis light illumination. This contributes to the hindering of electron–hole recombination, and thus, more electrons and holes can participate in the photocatalytic reaction.

Conflicts of interest

There are no conflicts to declare.

Acknowledgements

This work was supported by the Research Project of Education Ministry of Heilongjiang Province of China (135209223, 135209217, YSTSXK201843, 135309116). In addition, the authors also would like to express their gratitude to Research Project of the Ministry of Human Resources and Social Security of Heilongjiang Province of China (2018) and Research Project of the Ministry of Human Resources and Social Security of China (2015) for financial supports.

Notes and references

1 J. R. Chen, F. X. Qiu, W. Z. Xu, S. S. Cao and H. J. Zhu, *Appl. Catal., A*, 2015, **495**, 131–140.

2 N. Rahmani and R. S. Dariani, *J. Alloys Compd.*, 2016, **681**, 421–425.

3 X. Y. Niu, J. Y. Yu, L. K. Wang, C. F. Fu, J. X. Wang, L. Wang, H. L. Zhao and J. X. Yan, *Appl. Surf. Sci.*, 2017, **413**, 7–15.

4 J. A. Rengifo-Herrera, M. Blanco, J. Wist, P. Florian and L. R. Pizzio, *Appl. Catal., B*, 2016, **189**, 99–109.

5 J. L. Li, S. Q. Jia, G. Z. Sui, L. J. Du and B. X. Li, *RSC Adv.*, 2017, **7**, 34857–34865.

6 S. Dosta, M. Robotti, S. Garcia-Segura, E. Brillas, I. G. Cano and J. M. Guilemany, *Appl. Catal., B*, 2016, **189**, 151–159.

7 C. R. Jiang, K. Y. Lee, C. M. A. Parlett, M. K. Bayazit, C. C. Lau, Q. S. Ruan, S. J. A. Moniz, A. F. Lee and J. W. Tang, *Appl. Catal., A*, 2016, **521**, 133–139.

8 W. X. Li, T. Bak, A. Atanacio and J. Nowotny, *Appl. Catal., B*, 2016, **198**, 243–253.

9 L. Y. Shen, Z. P. Xing, J. L. Zou, Z. Li, X. Y. Wu, Y. C. Zhang, Q. Zhu, S. L. Yang and W. Zhou, *Sci. Rep.*, 2017, **7**, 41978–41984.

10 C. M. Tsai, C. G. Song, Y. C. Hung, Y. G. Jeong, S. H. Oh, J. H. Jeong, H. J. Kim, H. Huh, J. W. Yoon and W. Sigmund, *Ceram. Int.*, 2017, **43**, 3761–3768.

11 H. B. Li, Y. L. Ma and R. Niu, *Sep. Purif. Technol.*, 2016, **171**, 93–100.

12 V. R. Djokic, A. D. Marinkovic, O. Ersen, P. S. Uskokovic, R. D. Petrovic, V. L. R. Radmilovic and D. T. Janackovic, *Ceram. Int.*, 2014, **40**, 4009–4018.

13 C. S. Chen, N. Wang, P. Zhou, H. S. San, K. Y. Wang and X. Y. Chen, *ACS Appl. Mater. Interfaces*, 2016, **8**, 24638–24644.

14 J. L. Li, L. J. Du, S. Q. Jia, G. Z. Sui, Y. L. Zhang, Y. Zhuang, B. X. Li and Z. Y. Xing, *RSC Adv.*, 2018, **8**, 29645–29653.

15 G. D. Jiang, X. X. Yang, Y. Wu, Z. W. Li, Y. H. Han and X. D. Shen, *Mol. Catal.*, 2017, **432**, 232–241.

16 Z. W. Tong, D. Yang, T. X. Xiao, Y. Tian and Z. Y. Jiang, *Chem. Eng. J.*, 2015, **260**, 117–125.

17 L. Zhou, L. Z. Wang, J. Y. Lei, Y. D. Liu and J. L. Zhang, *Catal. Commun.*, 2017, **89**, 125–128.

18 Z. P. Chen, W. C. Ren, L. B. Gao, B. L. Liu, S. F. Pei and H. M. Cheng, *Nat. Mater.*, 2011, **10**, 424–428.

19 C. Dai, S. J. Zhang, Z. Liu, R. Wu and Y. Chen, *ACS Nano*, 2017, **11**, 9467–9480.

20 H. I. Kim, G. H. Moon, D. Monllor-Satoca, Y. Park and W. Choi, *J. Phys. Chem. C*, 2012, **116**, 1535–1543.

21 Y. Zhang, C. W. Foster, C. E. Banks, L. D. Shao, H. S. Hou, G. Q. Zou, J. Chen, Z. D. Huang and X. B. Ji, *Adv. Mater.*, 2016, **28**, 9391–9399.

22 M. H. Wang, L. F. Cai, Q. X. Jin, H. Z. Zhang, S. M. Fang, X. W. Qu, Z. H. Zhang and Q. Z. Zhang, *Sep. Purif. Technol.*, 2017, **172**, 217–226.

23 G. Mamba, M. A. Mamo, X. Y. Mbianda and A. K. Mishra, *Ind. Eng. Chem. Res.*, 2014, **53**, 14329–14338.

24 G. Ersan, O. G. Apul, F. Perreault and T. Karanfil, *Water Res.*, 2017, **126**, 385–398.

25 D. G. Papageorgiou, I. A. Kinloch and R. J. Young, *Prog. Mater. Sci.*, 2017, **90**, 75–127.

26 L. L. Jiang, X. Lu, C. M. Xie, G. J. Wan, H. P. Zhang and Y. H. Tang, *J. Phys. Chem. C*, 2015, **119**, 3903–3910.

27 M. C. Long, Y. L. Qin, C. Chen, X. Y. Guo, B. H. Tan and W. M. Cai, *J. Phys. Chem. C*, 2013, **117**, 16734–16741.

28 N. Zhang, Y. H. Zhang, X. Y. Pan, M. Q. Yang and Y. J. Xu, *J. Phys. Chem. C*, 2012, **116**, 18023–18031.

29 V. Stengl, D. Popelkova and P. Vlacil, *J. Phys. Chem. C*, 2011, **115**, 25209–25218.

30 R. Wang, Q. D. Wu, Y. Lu, H. W. Liu, Y. Z. Xia, J. Q. Liu, D. J. Yang, Z. Y. Huo and X. D. Yao, *ACS Appl. Mater. Interfaces*, 2014, **6**, 2118–2124.

31 X. Pan, Y. Zhao, S. Liu, C. Korzeniewski, S. Wang and Z. Y. Fan, *ACS Appl. Mater. Interfaces*, 2012, **4**, 3944–3950.

32 S. D. Perera, R. G. Mariano, K. Vu, N. Nour, O. Seitz, Y. Chabal and K. J. Balkus, *ACS Catal.*, 2012, **2**, 949–956.

33 L. A. Gu, J. Y. Wang, H. Cheng, Y. Z. Zhao, L. F. Liu and X. J. Han, *ACS Appl. Mater. Interfaces*, 2013, **5**, 3085–3093.

34 Q. W. Huang, S. Q. Tian, D. W. Zeng, X. X. Wang, W. L. Song, Y. Y. Li, W. Xiao and C. S. Xie, *ACS Catal.*, 2013, **3**, 1477–1485.

35 Y. H. Wu, P. Y. Tseng, P. Y. Hsieh, H. T. Chou and N. H. Tai, *ACS Appl. Mater. Interfaces*, 2015, **7**, 9453–9461.

36 X. M. Liu, M. Khan, W. X. Liu, W. Xiang, M. Guan, P. Jiang and W. B. Cao, *Ceram. Int.*, 2015, **41**, 3075–3080.

37 Y. Chen and K. R. Liu, *J. Hazard. Mater.*, 2017, **324**, 139–150.

38 M. A. Farrukh, M. Shahid, I. Muneer, S. Javaid and M. Khaleeq-ur-Rahman, *J. Mater. Sci.: Mater. Electron.*, 2015, **27**, 2994–3002.

39 Y. M. Yu, J. F. Geng, H. Li, R. Y. Bao, H. Y. Chen, W. Z. Wang, J. X. Xia and W. Y. Wong, *Sol. Energy Mater. Sol. Cells*, 2017, **168**, 91–99.

40 S. Paul, P. Chetri, B. Choudhury, G. A. Ahmed and A. Choudhury, *J. Colloid Interface Sci.*, 2015, **439**, 54–61.

41 M. Zalas, *J. Rare Earths*, 2014, **32**, 487–495.

42 D. Z. Lu, P. F. Fang, J. Q. Ding, M. C. Yang, Y. F. Cao, Y. W. Zhou, K. Peng, K. K. Kondamareddy and M. Liu, *Appl. Surf. Sci.*, 2017, **396**, 185–201.

43 W. J. Zhang, Y. X. Liu, X. B. Pei and X. J. Chen, *J. Phys. Chem. Solids*, 2017, **104**, 45–51.

44 W. D. Yang, Y. R. Li and Y. C. Lee, *Appl. Surf. Sci.*, 2016, **380**, 249–256.

45 J. L. Li, T. Liu, G. Z. Sui and D. S. Zhen, *J. Nanosci. Nanotechnol.*, 2015, **15**, 1408–1415.

46 Z. L. Cheng, X. J. Quan, J. X. Xiang, Y. M. Huang and Y. L. Xu, *J. Environ. Sci.*, 2012, **24**, 1317–1326.

47 P. H. Wang, *J. Environ. Sci.*, 2017, **56**, 202–213.

48 S. Y. Pu, R. X. Zhu, H. Ma, D. L. Deng, X. J. Pei, F. Qi and W. Chu, *Appl. Catal., B*, 2017, **218**, 208–219.

49 J. J. Zhang, X. Liu, T. Ye, G. P. Zheng, X. C. Zheng, P. Liu and X. X. Guan, *J. Alloys Compd.*, 2017, **698**, 819–827.

50 H. Safajou, H. Khojasteh, M. Salavati-Niasari and S. Mortazavi-Derazkola, *J. Colloid Interface Sci.*, 2017, **498**, 423–432.

51 M. Minella, F. Sordello and C. Minero, *Catal. Today*, 2017, **281**, 29–37.